



RESEARCH ARTICLE

10.1002/2014JB011766

Key Points:

- Reservoir loading caused significant CFS increase at shallow-middle depth
- Seismicity around reservoir showed progressive spatial expansion due to pore pressure diffusion
- Wenchuan earthquake was likely triggered indirectly by reservoir impoundment

Correspondence to:

Z.-K. Shen,
zshen@ucla.edu

Citation:

Tao, W., T. Masterlark, Z.-K. Shen, and E. Ronchin (2015), Impoundment of the Zipingpu reservoir and triggering of the 2008 M_w 7.9 Wenchuan earthquake, China, *J. Geophys. Res. Solid Earth*, 120, doi:10.1002/2014JB011766.

Received 11 NOV 2014

Accepted 13 SEP 2015

Accepted article online 16 SEP 2015

Impoundment of the Zipingpu reservoir and triggering of the 2008 M_w 7.9 Wenchuan earthquake, China

Wei Tao¹, Timothy Masterlark², Zheng-Kang Shen^{3,4}, and Erika Ronchin⁵
¹State Key Laboratory of Earthquake Dynamics, Institute of Geology, China Earthquake Administration, Beijing, China,

²Department of Geology and Geological Engineering, South Dakota School of Mines and Technology, Rapid City, South Dakota, USA, ³Department of Earth, Planetary, and Space Sciences, University of California, Los Angeles, California, USA,

⁴Department of Geophysics, School of Earth and Space Science, Peking University, Beijing, China, ⁵Institute of Earth Sciences Jaume Almera, Spanish National Research Council (Consejo Superior de Invees Científicas), Barcelona, Spain

Abstract Impoundment of the Zipingpu reservoir (ZR), China, began in September 2005 and was followed 2.7 years later by the 2008 M_w 7.9 Wenchuan earthquake (WE) rupturing the Longmen Shan Fault (LSF), with its epicenter ~12 km away from the ZR. Based on the poroelastic theory, we employ three-dimensional finite element models to simulate the evolution of stress and pore pressure due to reservoir impoundment, and its effect on the Coulomb failure stress on the LSF. The results indicate that the reservoir impoundment formed a pore pressure front that slowly propagated through the crust with fluid diffusion. The reservoir loading induced either moderate or no increase of the Coulomb failure stress at the hypocenter prior to the WE. The Coulomb failure stress, however, grew ~9.3–69.1 kPa in the depth range of 1–8 km on the LSF, which may have advanced tectonic loading of the fault system by ~60–450 years. Due to uncertainties of fault geometry and hypocenter location of the WE, it is inconclusive whether impoundment of the ZR directly triggered the WE. However, a small event at the hypocenter could have triggered large rupture elsewhere on fault, where the asperities were weakened by the ZR. The microseismicity around the ZR also showed an expanding pattern from the ZR since its impoundment, likely associated with diffusion of a positive pore pressure pulse. These results suggest a poroelastic triggering effect (even if indirectly) of the WE due to the impoundment of the ZR.

1. Introduction

The May 2008 M_w 7.9 Wenchuan earthquake (WE) occurred on the central segment of the Longmen Shan Fault (LSF) in western China [Zhang *et al.*, 2010, and references therein]. The LSF is a reverse fault separating the Tibetan plateau from the Sichuan basin, with a fault slip rate of 1–3 mm/yr [Zhang *et al.*, 2004; Shen *et al.*, 2005; Densmore *et al.*, 2007]. The earthquake initiated at about 14–19 km depth, propagated upward and mostly northeastward, producing a surface rupture of about 240 km long. The quake started with predominantly thrust motion on a modest dipping fault and changed into predominantly dextral slip on a steep dipping fault as the rupture propagated northeastward [e.g., Shen *et al.*, 2009; Fielding *et al.*, 2013]. This earthquake caused more than 90,000 casualties and became the most devastating natural disaster in China since the 1976 M_w 7.8 Tangshan earthquake.

Following the WE, it has been debated whether the quake was triggered by the impoundment of the nearby Zipingpu reservoir (ZR). The initial impoundment of the reservoir began in September 2005. By December 2005, the water level rose from an elevation of 760 m to 820 m and then reached a maximum elevation of 875 m in October 2006. For the following 2.5 years the water level remained elevated with a minimum of 817 m [Lei, 2010]. In May 2008, 2.7 years after the impoundment of the ZR, the WE occurred on the Longmen Shan Fault (LSF). The epicenter of the WE is only about 12 km away from the ZR (Figure 1, http://data.earthquake.cn/datashare/datashare_dzsb_query_new.jsp), the close proximity of the WE and impoundment of the ZR in both space and time prompts a hypothesis that the impoundment of the ZR triggered the WE. This hypothesis has been tested in studies presenting sometimes contrasting results [Klose, 2008, 2012; Lei *et al.*, 2008; Ge *et al.*, 2009; Kerr and Stone, 2009; Deng *et al.*, 2010; Gahalaut and Gahalaut, 2010; Lei, 2010].

After the WE, Lei *et al.* [2008] and Lei [2010] evaluated the changes of Coulomb failure stress (Δ CFS) induced by elastic and uncoupled poroelastic responses and assessed their role in manifesting local seismicity and potential impact on the WE. According to their results, Δ CFS on the LSF was increased by more than

©2015. The Authors.

This is an open access article under the terms of the Creative Commons Attribution-NonCommercial-NoDerivs License, which permits use and distribution in any medium, provided the original work is properly cited, the use is non-commercial and no modifications or adaptations are made.

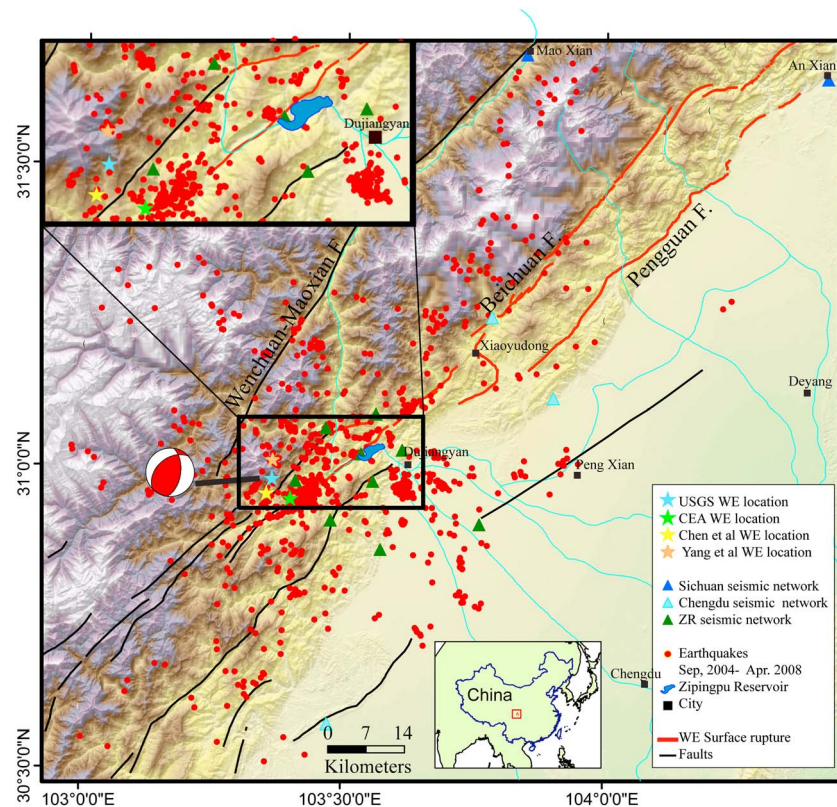


Figure 1. Tectonic setting of the ZR and WE. The lower inset map denotes the mapped region in China. The beach ball shows the U.S. Geological Survey (USGS) focal mechanism solution. The red dots show $M > 1.0$ earthquakes near the ZR between September 2004 and April 2008. The Zippingpu, Chengdu, and Sichuan seismic networks used to relocate the earthquakes are shown as green, light blue, and blue triangles, respectively. Red lines indicate surface traces of WE coseismic rupture. The main shock epicentral locations from the USGS, China Earthquake Administration (CEA), *Chen et al.* [2009], and *Yang et al.* [2012] are indicated by light blue, green, yellow, and orange stars, respectively. The blue irregular-shaped area in the upper inset map denotes the ZR.

0.1 MPa within 10 km beneath the reservoir and reached a few tens of kPa at the depth of 14 km. Such levels of ΔCFS are large enough to modulate a continuous secular stress buildup of a couple of hundreds of Pa/yr in the Longmen Shan thrust zone. *Klose* [2008, 2012] also calculated the ΔCFS on the Beichuan fault induced by the impoundment of the Zippingpu reservoir. Using a rate and state-dependent fault friction model, he estimated up to 60 years of advancement for the WE [*Klose*, 2012]. Another study by *Ge et al.* [2009] using an uncoupled poroelastic model concluded that the impoundment could have changed the Coulomb failure stress by up to 0.05 MPa at the reported hypocenters. They suggested that the impoundment of the ZR hastened the occurrence of the WE by tens to hundreds of years. Alternatively, *Deng et al.* [2010] and *Gahalaut and Gahalaut* [2010], using fluid flow models, estimated that the ΔCFS prior to the WE at the hypocenter on the fault was only on the order of 10^{-2} KPa and -0.2 to -0.5 KPa, respectively, and concluded that such changes are not large enough, or even negative, to have a triggering effect of the WE.

The idea that impoundments of some large reservoirs may have triggered earthquakes has been studied for decades [*Hagiwara and Ohtake*, 1972; *Gupta and Chadha*, 1995; *Talwani*, 1997; *Guha*, 2000]. The effect of reservoir loading on the existing stress field is a convenient mechanism to account for local earthquakes in the wake of reservoir impoundment. However, a time delay was often observed; i.e., higher seismicity pattern would not appear until several years after the initial impoundment, suggesting mechanism(s) other than the initial elastic response to reservoir loading [*Talwani and Acree*, 1984; *Talwani*, 1997]. *Roeloffs* [1988] evaluated stress and pore pressure changes in a uniform poroelastic half-space model produced by reservoir loading. *Kuslala and Talwani* [1992] calculated stress changes resulted from both elastic response and changes in pore pressure due to reservoir impoundment. They found that the elastic response may either stabilize or destabilize the reservoir environment, depending on the nature of preexisting stress field and the relative

geometry of the reservoir to the fault and the faulting mechanism. However, the increase in pore pressure along a given fault always leads to weakening, facilitating the onset of seismicity [Kuslala and Talwani, 1992]. Therefore, it is the pore pressure diffusion that is principally responsible for reservoir-induced seismicity [Talwani, 1997].

Mechanical coupling between the stresses of the rock matrix and the fluid pressure in the pore spaces (pore pressure) plays an important role in manifesting the stress field in saturated porous media. However, previous studies treated the stress and pore pressure fields induced by the impoundment of the ZR as either uncoupled or decoupled. An uncoupled problem is one in which the elastic stresses and pore pressure are independent of each other. A decoupled problem is one in which the elastic stresses influence pore pressure but not vice versa [Roeloffs, 1988; Kalpna and Chander, 2000]. If the fluid flow problem was solved independent of the stress field, the solution would be a mathematically simpler scalar field of pore pressure. The level of mathematical difficulty in solutions increases vastly from uncoupled to coupled problems, for which the latter includes a scalar pore pressure field that is coupled to a vector field of displacement. In this paper we study the possible relationship between the ZR and the WE using fully coupled poroelastic models.

Earthquakes can be triggered by transient stress changes, either tectonically or nontectonically. It is, however, a challenge to establish the causal relationship between a transient signal and earthquake occurrence. Multiple techniques have been developed in recent years for the task, using statistical or mechanical tools based on seismicity and/or other data (e.g., see Cesca *et al.* [2013] and Dahm *et al.* [2013] for summary). A temporal delay during the process could be the result of viscoelastic deformation in the media, and/or rate and state-dependent friction on fault [e.g., Hainzl *et al.*, 2010]. Employing such a model to analyze ZR impoundment and seismicity data observed before the WE, Klose [2012] reported a positive correlation between reservoir impoundment and seismicity during some time periods since impoundment and Lei [2010] found three clusters of microseismic events occurred in areas with impoundment induced ΔCFS increased by > 0.01 MPa.

2. Method and Model

2.1. Coulomb Failure Stress Change

Coulomb failure criterion is a widely used criterion to characterize the change in tendency for frictional slip along a preexisting incipient fault plane [e.g., King *et al.*, 1994; Cocco and Rice, 2002]. The change in Coulomb failure stress is defined as

$$\Delta CFS = \sigma_s + \mu(\sigma_n + P) \quad (1)$$

where σ_s is the incremental change in shear stress (in favor of the slip direction-positive); σ_n is the incremental change in fault-normal stress (extension-positive); P is the incremental change in pore pressure; and μ is the coefficient of friction, which ranges between 0.6 and 0.85 for most rocks [Byerlee, 1978, 1992; Harris, 1998]. We use the median value $\mu = 0.7$ in this study. A positive change in ΔCFS promotes failure and negative change increases stability of the fault.

The second term on the right side of equation (1) that is scaled by the friction coefficient is the incremental change in effective normal stress (σ_{effn}). In this paper we calculate the pore pressure, shear stress, and normal stress and evaluate the ΔCFS by studying the change of shear stress and effective normal stress. The increase of either shear stress or effective normal stress induces the increase of the ΔCFS .

In a study about whether the 1992 Landers earthquake changed the proximity to failure on the San Andreas fault system, King *et al.* [1994] estimated that a ΔCFS increase in the range of 100–600 kPa could trigger or hasten the next great earthquake there by about a decade. Stein [1999] came to a conclusion that a small, sudden stress increase by ~ 10 kPa on a fault could cause 20–25% increase of shocks, which is statistically significant. Cochran *et al.* [2004] studied the correlation between the occurrence of shallow thrust earthquakes and that of the strongest tides and found significant increase in triggering of globally distributed large events ($M > 5.5$) by solid Earth tide stresses, with associated ΔCFS increases of up to 5 kPa. It is therefore important to evaluate not only the sign change but also the magnitude of ΔCFS for assessing its possible triggering effect.

2.2. Fully Coupled Poroelastic Theory

We employ fully coupled poroelastic analysis. The governing equations for a three-dimensional media are

$$G\nabla^2 u_x + \frac{G}{1-2\nu} \left(\frac{\partial^2 u_x}{\partial x^2} + \frac{\partial^2 u_y}{\partial x \partial y} + \frac{\partial^2 u_z}{\partial x \partial z} \right) = \alpha \frac{\partial P}{\partial x} - F_x \quad (2)$$

$$G\nabla^2 u_y + \frac{G}{1-2\nu} \left(\frac{\partial^2 u_x}{\partial x \partial y} + \frac{\partial^2 u_y}{\partial y^2} + \frac{\partial^2 u_z}{\partial y \partial z} \right) = \alpha \frac{\partial P}{\partial y} - F_y \quad (3)$$

$$G\nabla^2 u_z + \frac{G}{1-2\nu} \left(\frac{\partial^2 u_x}{\partial x \partial z} + \frac{\partial^2 u_y}{\partial y \partial z} + \frac{\partial^2 u_z}{\partial z^2} \right) = \alpha \frac{\partial P}{\partial z} - F_z \quad (4)$$

$$\frac{k}{\mu} \nabla^2 P + S_e \frac{\partial P}{\partial t} = \alpha \frac{\partial \varepsilon_{kk}}{\partial t} + Q \quad (5)$$

where u is displacement, G the shear modulus, ν the Poisson's ratio, F a vector body force per unit volume, k the permeability, μ the fluid viscosity, S_e the constrained specific storage coefficient, ε_{kk} the volumetric strain, α the Biot-Willis coefficient, Q the fluid source, and t the time [Wang, 2000]. The first three equations (2)–(4) are achieved by substituting the constitutive elastic relationships and strain-displacement definitions into the force balance equations. The fourth equation (5) is derived using the principles of fluid continuity and Darcy's law [Wang, 2000]. Notice that the pore pressure terms in (2)–(4) and volumetric strain term in (5) couple the pore pressure and stress fields.

2.3. Three-Dimensional Finite Element Model

The geometry of the model domain is simplified from the regional geologic configuration near the ZR and the LSF. One of the horizontal coordinate axes (y axis) has a strike of $N42^\circ \pm 5^\circ E$ (Figure 1) following the field survey of the WE surface offset [Xu et al., 2009], and the vertical (z) axis of the domain is upward positive, with respect to the Earth surface. The other horizontal coordinate (x) axis is orthogonal to the strike of the surface offsets of the LSF. The model domain simulates a surface area of $300 \text{ km} \times 250 \text{ km}$ and a thickness of 100 km and is meshed into 464,580 first-order hexahedron elements (Figure 2). The characteristic element lengths are 100 m near the simulated fault and the reservoir, and $10,000 \text{ m}$ at far-field boundaries. This three-dimensional domain is partitioned into mantle and crust regions. We assume that the crust region in the model is represented by a poroelastic material having a permeability that decreases as a function of depth. As shown in Figure 1, the surface shape of the reservoir in field is an approximate oval with a 5 km major axis parallel to and a 2 km minor axis normal to the WE surface rupture. From the loading history, the average water head was $\sim 100 \text{ m}$ [Lei et al., 2008; Ge et al., 2009]. Therefore, the reservoir is simplified as a half triaxial ellipsoid with the horizontal axes of 5 km and 2 km and the vertical semiaxis of 100 m embedded in the model surface.

Permeability is an intrinsic property of the rock. Ingebritsen and Manning [1999, 2010] estimated the permeability variation with depth in continental crust based on hydrothermal modeling and progress of metamorphic reactions driven by fluid flow. They combined geothermal and metamorphic data and determined that the mean permeability (k) of tectonically active continental crust decreases with depth following $\log k \approx -14 - 3.2 \log(-z)$, where k is in square meters, z is the depth in kilometers and upward positive. Field permeability measurements and lab experiments at high pressure and temperature by Shmonov et al. [2003] yield a similar relation, $\log k \approx -12.56 - 3.225(-z)^{0.223}$, again with k in square meters and z in kilometers upward positive, respectively. These studies suggest that the permeability decreases much faster with depth in the upper crust than in the lower crust. We use a depth-dependent permeability structure according to the above studies. This permeability is recast into a corresponding hydraulic conductivity (K) structure for convenience:

$$K = \frac{\rho g}{\mu} k \quad (6)$$

where ρ is the fluid density and g the gravitational acceleration [Wang, 2000]. Assuming that the viscosity of water μ is 10^{-3} Pa s , the density of water is 1000 kg/m^3 , and acceleration of gravity is 10 m/s^2 , the hydraulic conductivity is proportional to permeability by a factor of 10^7 . Considering that the permeability in thick crust may vary by a few orders of magnitude, variation of viscosity of water with depth could be ignored in this study.

We use Abaqus software version 6.9-EF (www.simulia.com) to simulate this model configuration. The poroelastic properties of Westerly Granite [Wang, 2000] are used to represent the poroelastic crust. The mantle is

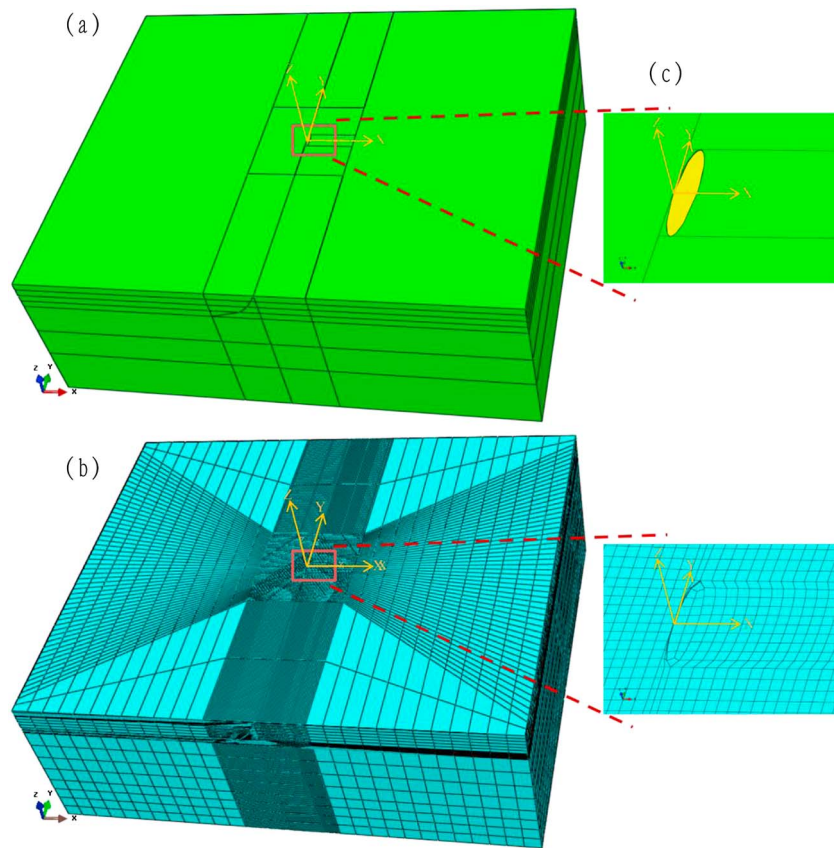


Figure 2. Finite element method (FEM) model configuration. (a) The 3-D domain is partitioned into mantle and crust regions. The crust is further partitioned to five layers. Corresponding material properties are listed in Table 1. (b) FEM model mesh contains 481,989 nodes and 464,580 elements. (c) Blow-up view of the FEM model mesh near reservoir. Yellow ellipse indicates the location of the ZR load.

treated as simple elastic material. We ignore viscoelastic relaxation in the mantle, because (1) the viscoelastic response to the relatively slow tectonic convergence is insignificant during the relatively short duration separating the impoundment of the ZR and WE, and (2) the magnitude and small spatial footprint of the ZR load introduces negligible differential stresses in the mantle. We use elastic properties of dunitite to represent the mantle [Turcotte and Schubert, 2002]. To be clear, we assume that the mechanical properties from these representative rocks are valid for our model domain, rather than imply that these specific rocks are found in the actual region of the study site. The material properties of the poroelastic crust and elastic mantle are summarized in Table 1.

Table 1. Material Properties

	Depth Range (km)		Poisson's Ratio	Young's Modulus (Pa)	Hydraulic Conductivity (m/s)	Bulk Modulus of Granite (Pa)	Bulk Modulus of Water (Pa)
	Tibet	Sichuan Basin					
Crust_1 (Westerly granite) ^a	0–5	0–5	0.25	3.75e10	1.0e–8	4.2e10	2.2e9
Crust_2 (Westerly granite) ^a	5–10	5–10	0.25	3.75e10	3.16e–10	4.2e10	2.2e9
Crust1_3 (Westerly granite) ^a	10–15	10–15	0.25	3.75e10	3.6e–11	4.2e10	2.2e9
Crust_4 (Westerly granite) ^a	15–20	15–20	0.25	3.75e10	1.0e–11	4.2e10	2.2e9
Crust_5 (Westerly granite) ^a	20–65	20–43	0.25	3.75e10	2.5e–12	4.2e10	2.2e9
Mantle (Dunit) ^b	65–100	43–100	0.36	1.4e11			

^aReference by Wang [2000].

^bReference by Turcotte and Schubert [2002].

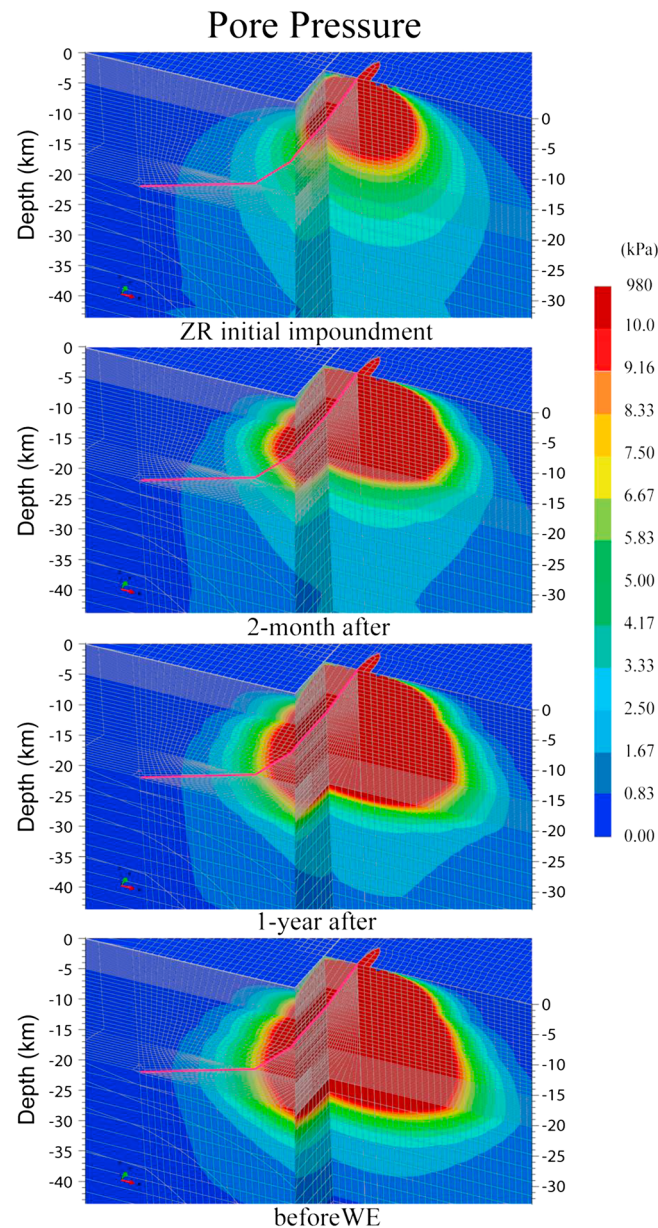


Figure 3. Spatial evolution of pore pressure after impoundment of ZR. The pink curve denotes the LSF. The right cross section cuts through the ZR, and the left cross section cuts through the USGS WE hypocenter location, respectively.

of the ZR. This transient postimpoundment interval is characterized by the convergence of the excess pore pressure field to steady state conditions constrained by the far-field boundary conditions and the pore pressure load of the reservoir. The constant and positive pore pressure boundary condition of the reservoir since the impoundment produces a positive pore pressure front that propagates outward from the reservoir and reaches the shallow part of the LSF first. In a few years, the pore pressure front propagates slowly through the crust and intersects the hypocentral region of the LSF (Figure 3). The timing of intersection of the pore pressure front with the LSF is controlled by the transient pore pressure field, depth-dependent hydraulic conductivity, and relative geometry of the listric LSF to the reservoir.

The hypocenter location of the WE was determined using various seismic data sets. Early results were from the USGS (<http://earthquake.usgs.gov/earthquakes/eqinthenews/2008/us2008ryan/>) using teleseismic data

The poroelastic modeling requires both displacement and fluid boundary conditions. The surface of the poroelastic region is stress-free with zero hydrostatic pressure beyond the reservoir region. The nodes corresponding to the boundaries of ZR are loaded with pressure of $P = \rho g z$ at the base of the reservoir, corresponding to the semiellipsoidal depth distribution of the ZR, that culminates to a maximum pressure at $z = -100$ m. The lateral boundaries are sufficiently far from the region of interest such that zero displacement and pore pressure are assumed there. The base of the poroelastic crust is simulated as zero flux. The initial conditions are assumed equilibrium stress and pore pressure.

The first modeling time step simulates the relatively instantaneous response to the impoundment of the ZR. The result of the first loading step serves as the initial conditions for the following modeling step, which also preserves these boundary and loading conditions and simulates the transient response of the system during the two-and-a-half-year interval separating the impoundment of the ZR (the first modeling step) and the initiation of the WE.

3. Results

3.1. Evolution of Pore Pressure

The model simulates the impoundment of the ZR as an instantaneous surface load that produces an undrained response that is localized to the region immediately beneath the ZR (Figure 3). Following the initial loading, pore fluids flow in response to the initial pore pressure field induced by the impoundment

Table 2. The Fault Plane and Source Parameters of WE Given by Focal Mechanism Solutions

Source	Latitude (°N)	Longitude (°E)	Depth (km)	Strike (°)	Dip (°)	Rake (°)
Yang <i>et al.</i> [2012]	31.018	103.365	15.5	/	/	/
Chen <i>et al.</i> [2009]	30.9607	103.3523	18.8	/	/	/
USGS	30.986	103.364	19	/	/	/
CEA	31.0	103.4	14	/	/	/
Hu <i>et al.</i> [2008]	31.00	103.40	14	202	27	90
Cui <i>et al.</i> [2011]	30.99	103.48	12.9	190	28	77
Guo <i>et al.</i> [2010]	/	/	/	247	62	131

and from CEA (http://data.earthquake.cn/datashare/datashare_dzsb_query_new.jsp) using regional seismic data, respectively. Later studies by Hu *et al.* [2008], Chen *et al.* [2009], Cui *et al.* [2011], and Yang *et al.* [2012] estimated the hypocenter location and/or the focal mechanism using different regional seismic data sets, respectively (Table 2). We illustrate in Figure 4 the evolution of predicted pore pressure changes at four hypocentral regions located by CEA, USGS, Chen *et al.* [2009], and Yang *et al.* [2012], and positions underneath the reservoir at the depths of 15 and 19 km. Among the four results the USGS study was determined using teleseismic body wave data and the rest by regional first arrival data, respectively. Generally speaking, the regional seismic data can provide better constraints for hypocenter location and earthquake mechanism solution. The results derived from the regional seismic data, however, are quite scattered (Figure 1 and Table 2), possibly caused by errors in seismic velocity structure of a highly heterogeneous crust surrounding the LSF. We therefore evaluate the pore pressure change and the ΔCFS at a wide range of scenario, taking into account possible ranges of the WE hypocenter source parameters such as the depth, location, and fault dip.

Our result shows that the pore pressure increases with time at all positions. The deeper in the crust and farther away from the reservoir, the slower the pore pressure increases, which is because of both the decrease of depth-dependent hydraulic conductivity and the reduced pressure gradient away from the source. The initial pore pressure change in response to the impoundment of the ZR reaches about 7 and 4.5 kPa at the depths of 15 and 19 km underneath the reservoir, and about 3, 2, 2, and 2 kPa at the WE hypocenters reported by CEA, USGS, Chen *et al.* [2009], and Yang *et al.* [2012]. Before the WE, the pore pressure further increased by 41 and 24 kPa at the depths of 15 and 19 km beneath the ZR, and 11.5, 6.5, 7.5, and 4.0 kPa at the CEA, USGS, Chen *et al.*, and Yang *et al.* reported hypocenters, respectively (Figure 4).

3.2. Evolution of ΔCFS

The fault geometry and dip angle impact the calculation of Coulomb failure stress. The geometry of the LSF is generally listric with high dip angles near the land surface [Burchfiel *et al.*, 2008], but the details are complex and vary along the strike of fault [Jia *et al.*, 2010]. Previous studies of the earthquake mechanism solution

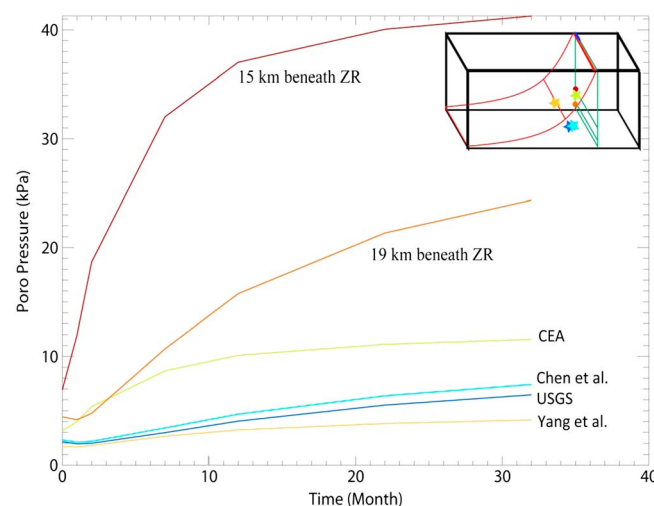


Figure 4. Temporal evolution of pore pressure predicted by FEM model. The inset sketch shows locations of evaluation sites.

yielded the hypocenter at 14–19 km depth range with the fault dip estimated 27°–62° (Table 2), which are averaged to a mean depth of 15.7 km and fault dip of 39°. Constrained by the fault drilling result of the Wenchuan Fault Scientific Drilling project, the near-surface fault dip angle is about 64° [Li *et al.*, 2013]. Using the above data as model constraints, we devise a continuous function f_z to describe the shape of the fault with depth:

$$f_z = \frac{2a}{\pi} \arctan\left(\frac{x}{b}\right) \quad (7)$$

where f_z is the depth of the fault plane and x is the horizontal distance from the fault surface trace. The two parameters are resolved as $a = 29.8$ km

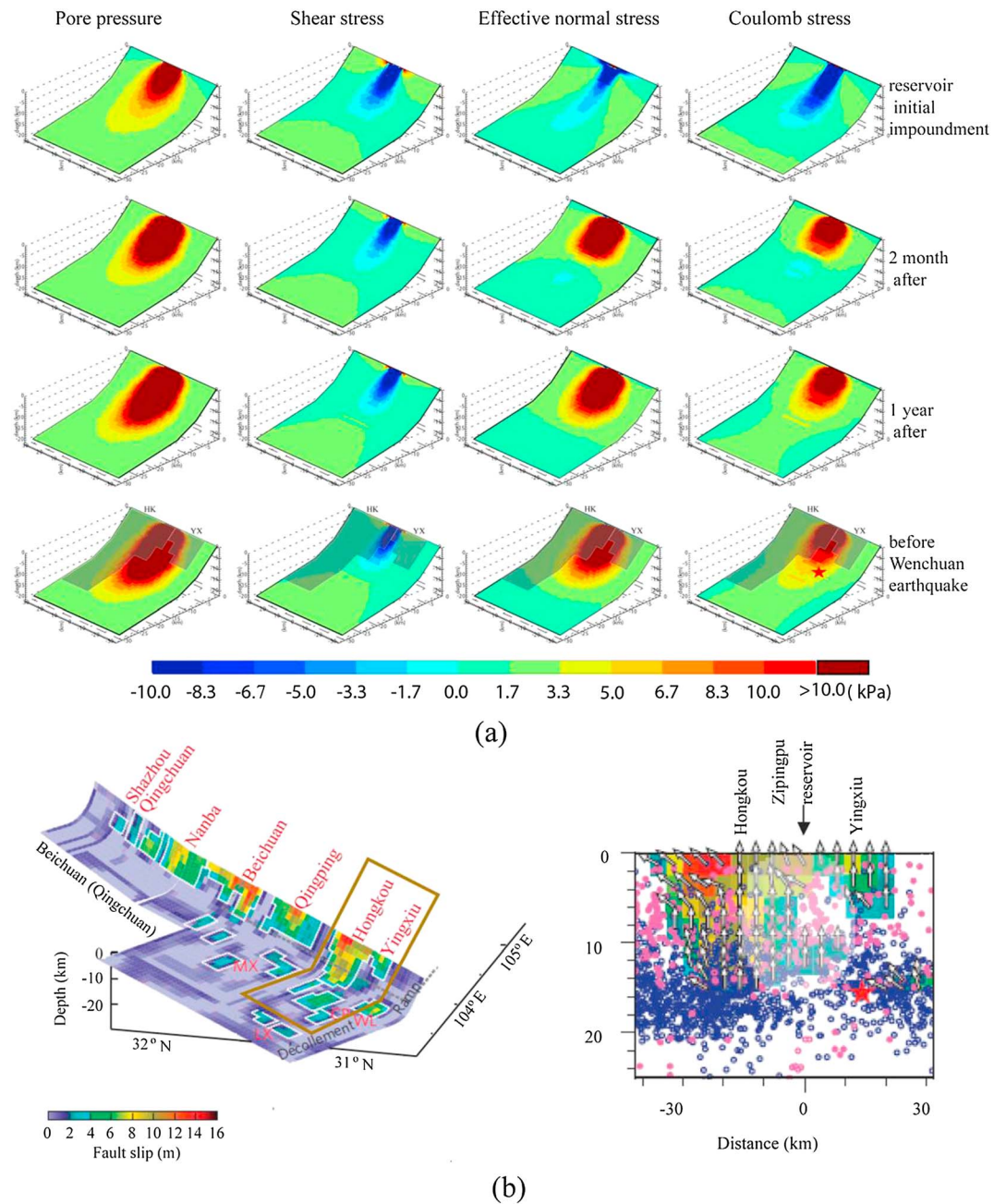


Figure 5. (a) Pore pressure, shear stress, normal stress, and Δ CFS distributions on fault plane of LSF. The stresses are plotted from -10.0 kPa to 10.0 kPa using the rainbow legend, and dark red and dark blue colors indicate the stresses off the positive or negative limit, respectively. The red star denotes the location of CEA reported hypocenter. The shadows on the fault plane (a, bottom row) indicate areas with >2 m coseismic slip determined by Wang *et al.* [2011]. (b, left) Coseismic slip distribution on the LSF by Wang *et al.* [2011]. (b, right) Blow-up view of slip at the Hongkou and Yingxiu asperities (area delineated by a green rectangle (b, left)), with the white shadow region denoting the area with >10 kPa of pore pressure increase prior to the WE.

and $b=9.2$ km. This model, nevertheless, is only an approximation for the fault geometry, and fault models within a reasonable range of geometry parameters are also explored.

The modeled evolution of the pore pressure, shear stress, effective normal stress, and Δ CFS on the fault plane are presented in Figure 5. The result shows that the shear stress on the fault plane does not change much after the impoundment of ZR, because it is the gravity loading of ZR that impacts the main part of the shear

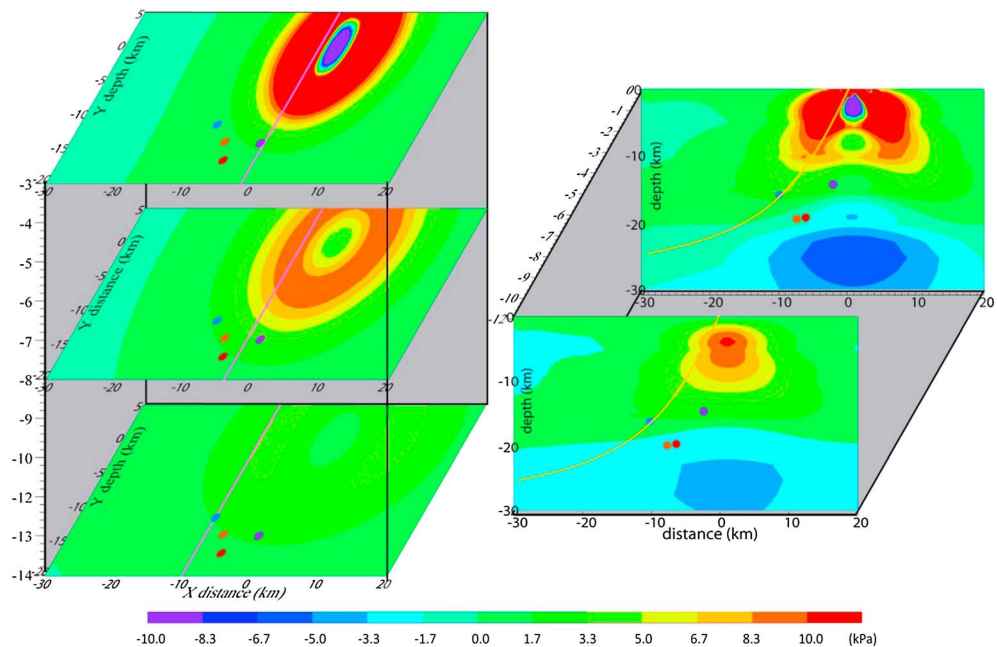


Figure 6. Δ CFS on cross sections in the crust. The Δ CFS is calculated assuming the same dip angle off the LSF as the dip angle on the LSF at equal depth. The stress is plotted from -8.3 kPa to 10.0 kPa using the rainbow legend. Red and purple colors indicate the stresses off the positive or negative limit, respectively. The blue, red, orange, and purple dots mark the WE hypocenter locations reported by CEA, USGS, Chen et al., and Yang et al., respectively.

stress change and is not very large. However, the effective normal stress increased significantly after the impoundment of ZR due to the increasing pore pressure. Initially, the effective normal stress is negative on the shallow part of the fault plane. After 2 months of impoundment, it has reversed to positive and then spread downward and outward on the fault plane. Therefore, the Δ CFS on the fault plane increases with time significantly, and its spreading pattern is similar to that of the effective normal stress. Initially, the Δ CFS is negative on the updip of the fault near the ZR and then reverses to positive and propagates downward and outward on the fault plane after a few months. Before the WE (2.7 years after), the Δ CFS is at its maximum of 365.2 kPa at 0 km depth on fault and decreases gradually downdip, reaching 69.1 , 27.5 , 17.8 , 9.3 , 4.7 , and 0.6 kPa at the depths of 1 , 2 , 5 , 8 , 12 , and 18 km, respectively (Figure 5).

To demonstrate how the stress field in crust has been disturbed by the impoundment of the ZR, we plot the Δ CFS cross sections prior to the WE on X-Y and X-Z planes that cut through the LMS fault, and the ZR or the WE hypocenter location in Figure 6. For the regions off the fault, dip angles and senses of slip directions are assumed the same as that on the fault plane at the same depth for Δ CFS calculation. The cross-section results indicate negative Δ CFS in a narrow area underneath the ZR within the depth of 4 km. With that exception, the Δ CFS increases more than 10 kPa within the depth of 10 km around the ZR. The Δ CFS in the crust deeper than 20 km is negative, due to elastic loading of the ZR and minimal pore pressure change. The Δ CFS between the depths of 10 and 20 km increases from 10 to 0 kPa. At the reported hypocenters, the Δ CFS increases about 2 kPa at the CEA and Yang et al. reported locations, and close to 0 at the USGS and Chen et al. reported locations. In the vicinity of the fault plane in the 5 – 15 km depth range, the Δ CFS increases about 20% 2 km east of the fault and decreases about 20% 2 km west of the fault, respectively, suggesting noticeable effect of fault geometry uncertainty to Δ CFS estimates.

Considering of the uncertainty of the rupturing plane geometry, we further examine effect of fault dip angle to the estimate of Δ CFS at the WE hypocenter before the quake (Figure 7). For the fault dip angle increasing from 10° to 70° , the Δ CFS changes from -2 kPa to over 8 kPa at the CEA reported WE hypocenter, from -4 kPa to 4 kPa at the USGS and Chen et al. reported hypocenters, and from -2 kPa to 4 kPa at the Yang et al. reported hypocenter, respectively. For the more likely dip angle range of 25° to 45° , the Δ CFS varies from -2.5 kPa to 4 kPa at the reported hypocenters, suggesting the Δ CFS to have either a moderate or no triggering effect.

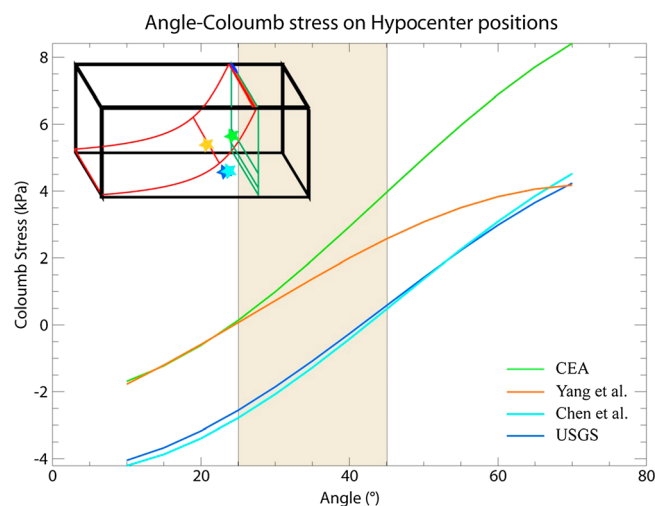


Figure 7. Δ CFS versus fault dip angle at reported WE hypocenters. The green, blue, light blue, and orange curves are Δ CFS at the CEA, USGS, Chen et al., and Yang et al. reported hypocenters. The inset sketch shows locations of the reported hypocenters marked as stars in model setting, whose colors correspond to the colors of the curves.

4. Discussions and Conclusions

In this study we have addressed several important factors associated with the Δ CFS estimation around the LSF that were considered to some extent in previous studies, such as the following: (1) Larger diffusivity in crust would result in faster pore pressure front propagation and larger Δ CFS on fault [Lei et al., 2008; Lei, 2010; Ge et al., 2009; Gahalaut and Gahalaut, 2010]. (2) If the undrained response pressure was not considered, the final pore pressure would be underestimated, along with the estimate of Δ CFS [Ge, 2011]. (3) The Δ CFS estimate is affected significantly by the fault dip angle, and at the same hypocentral location, higher dip angle would result in greater Δ CFS [Zhou and Deng, 2011]. (4) In all the depth range

studied, the pore pressure increase due to 2.7 years of diffusion after the impoundment of ZR is greater than the initial pore pressure jump due to the static loading of the reservoir (Figure 4) [Ge, 2011]. (5) A 2-D model would overestimate the predicted Δ CFS due to 3-D out-of-plane stress and pore pressure variations [Gahalaut and Gahalaut, 2010]. Because each of the previous studies chose the aforementioned model parameters somewhat differently, the results from these studies are inevitably somewhat different.

Some other parameterizations can also make significant differences. For example, in our study the shape of the reservoir is approximated as a half oval with the three semiaxes as 2.5 km, 1.0 km, and 0.1 km respectively, approximated from the reservoir geometry data. In contrast, Ge et al. [2009] utilized a 2-D model and assumed a rectangular cross section for the reservoir with 5 km \times 0.1 km in size. Without accounting the 2-D versus 3-D model difference this disparity in loading source modeling would already cause a factor of 3 differences in undrained pore pressure estimation; and the drained pore pressure would also be significantly affected.

Another and perhaps even greater factor affecting the triggering effect of the ZR is the location and dip angle of the fault where the Δ CFS should be evaluated. If the initial triggering had to be on a fault which has the same dip angle as of the LSF that ruptured during the WE and is listric in shape, the Δ CFS distribution pattern would be similar to that of Ge et al. [2009] and also of this study; i.e., positive Δ CFS in the hanging wall, and negative Δ CFS in parts of the footwall region, particularly where immediate underneath the ZR and more than 20 km in depth. Depending on the assumption of hypocentral location of the WE—on or off the fault and in the depth range, the Δ CFS estimate would vary greatly, or even change the sign (Figure 6). This is perhaps the primary reason why different models would produce so much different or even opposite model results and interpretations.

One factor which may also have a significant impact on the result are the physical properties of the fault zone, which can be highly heterogeneous. For example, laboratory experiments showed that the presence of fracture could make the crust rock sample 4–7 orders of magnitude more permeable than the host rock [Durham, 1997; Miller, 2013]. If a fault zone is composed of such fractured rocks, water could diffuse at much faster rates downward through the fault zone, and the result presented above would have to be altered appreciably. Key to the issue is the physical parameters of the fault zone: its permeability, width, and connectivity. Unfortunately, all the parameters are poorly known, particularly for fault zone materials down to midcrust depths. We, however, envision that the fault zone fracture might not have played a significant role in triggering the WE for two reasons. (a) The Minjiang River flows along a stretch of the LSF for about 10 km (Figure 1); if the diffusive effect on fault is significant, water should have saturated the fault zone underneath this stretch of the fault and beyond over geological time, contribution from the 2.7 years impoundment of the ZR would

become relatively less important. (b) Coseismic fault slip distribution revealed that fault slip was largest at shallow depth underneath the ZR [Shen *et al.*, 2009; Wang *et al.*, 2011], suggesting that the fault was locked at shallow depth prior to the WE. Such a result does not seem to lend support to a fault zone model which is connected and lubricated at shallow depth by water saturation.

Moreover, among the previous studies, although the Δ CFS estimates on hypocenters were different, the projections of the Δ CFS increase in shallow part of the crust around the ZR were consistently large, on the order of tens to hundreds of kPa. Wang *et al.* [2014], using GPS data as model constraints, estimated the tectonic stress loading rate on the LSF as of ~ 155 Pa/yr. The 69.1, 17.8, 9.3, and 4.7 kPa Δ CFS increases estimated at the depths of 1, 5, 8, and 12 km due to the ZR impoundment are therefore equivalent to ~ 446 , ~ 115 , ~ 60 , and ~ 30 years of advancement of earthquake recurrence time at these depths, respectively. The ZR happened to be positioned on top of asperities on the LSF. In Figure 5 we plot spatial distribution of >2 m slip of the WE on the fault, resolved from geodetic data inversion by Wang *et al.* [2011]. As shown in the figure, the region with significant increase of Δ CFS on the LSF embraces two asperities ruptured during the WE from middle to shallow depth, one is under the Yingxiu city and the other under the Hongkou town (Figure 5). The WE started near Yingxiu, and the hypocenter is underneath the Yingxiu asperity (Figures 5 and 7). Slip of the Hongkou asperity peaked at ~ 7 m at surface and was measured as one of the largest slip regions for the entire WE rupture [Xu *et al.*, 2009]. As we have discussed above, the most important impact of the impoundment of the ZR might be to have advanced these asperities toward failure. Once an asperity failed, it could trigger rupturing of other asperities on the LSF in a run-away cascade style, as occurred during the WE [Shen *et al.*, 2009]. Therefore, even the initial failure might not have been necessarily induced by the ZR, a small event at the deeper section of the fault could be triggering rupture of asperity at upper section of the fault, which was weakened by the impoundment of the ZR.

To further assess the triggering effects of the impoundment of the ZR, we analyze microseismic activities around the ZR during the period between the impoundment of the ZR and the occurrence of the WE. If the pore pressure changes due to the impoundment of the ZR did trigger, directly or indirectly, the WE, the same mechanism should also trigger local microseismic activities and show in their spatiotemporal evolution pattern.

A seismic network composed of seven short-period seismometers was deployed in July 2004 (about 1 year before construction of the ZR) began to monitor microseismic activities around the ZR. The average spacing between neighboring stations is about 10 km (the network geometry is shown in Figure 1). Using the data from the ZR seismic network, combined with data recordings from a regional seismic network operated by the Sichuan Seismological Bureau (the site locations are also shown in Figure 1), Ma *et al.* [2011] relocated the microearthquakes around the ZR using the double-difference relocation algorithm. We adopt these data for seismicity analysis in this study.

We display the earthquakes relocated ($M \geq 0.1$) in Figures 1 and 8. Between September 2007 and February 2008, the earthquakes swarmed at two places, one is near the southwest end of the surface rupture of the WE and the other about 10 km northeast of the ZR. In a fault cross section, on the southwest side of the ZR, the microearthquakes illuminate the shallow part of the LSF (Figure 8). A swarm of microevents occurred about 8 km from and southeast of the ZR at 13–15 km depth, which may indicate a weak zone on the fault. The time period that most of the microevents occurred in the swarm is around 2–2.5 years after the impoundment, suggesting that in this time period the pore pressure change may have diffused to and exerted triggering effects on local preexisting structures around the LSF.

For a close examination of time-distance effect of pore pressure propagation, we divide the microearthquakes in groups by 6 month time segments before and after the impoundment of the ZR, sort the local earthquakes (within 20 km from the ZR) by their distances to the ZR in each time segment, and plot the cumulative histogram of the events as a function of the distance to the ZR (Figure 9). The slope of each cumulative histogram in Figure 9 is then proportional to the earthquake occurrence rate at the time and distance, and a higher slope indicates greater seismicity per distance range (higher seismicity density). Consequently, the time-distance evolution process of the earthquakes among different time periods would be highlighted by the evolution of prominent slopes on the curves of different time segments. Before impoundment of the ZR, for the two curves of B1 and B2 (0–0.5 years and 0.5–1 years since the start of data recording), the highest slopes are located within 5 to 10 km away from the ZR (indication of microseismicity in the vicinity of the LSF).

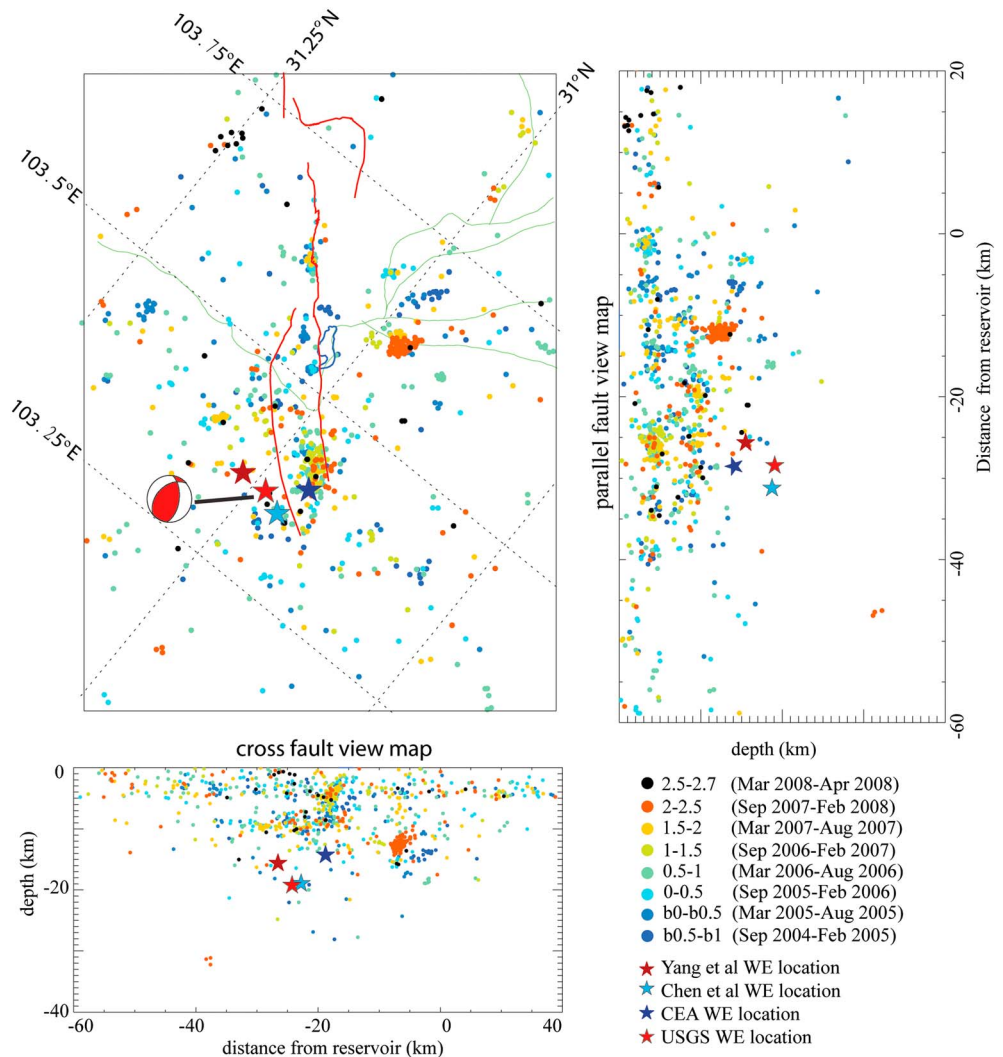


Figure 8. Spatial distribution of the microearthquakes observed in the ZR region between September 2004 and April 2008. Events are colored based on their time of occurrences. (a–c) The events in map view and in vertical cross sections along and perpendicular to fault strike, respectively. The red, dark red, blue, and light blue stars show locations of the USGS, Yang et al., CEA, and Chen et al. reported hypocenters and the beach ball the USGS focal mechanism solution, respectively.

After impoundment of the ZR, the highest slopes for the rest of the curves, which indicate the highest seismicity density region in each time segment, however, are progressively located at further distances. By the chronological order of the curves, the highest seismicity density region are located away from the ZR at 9.5–12 km for C1 (0–0.5 years), 13–15 km for C2 (0.5–1 years), 13–16 km for C3 (1–1.5 years), 14–17 km for C4 (1.5–2 years), and 15–20 km for C5 (2.5–2.7 years). Although the slope of C4 is dictated predominantly by an earthquake swarm located within the distance of 14–17 km from the ZR, the microseismic activities prior to the WE still shows a consistent pattern associated with the outward diffusion of pore pressure from the ZR.

In summary, comparing to previous studies we have achieved the following: (a) used a fully coupled poroelastic model to do the FEM simulation; (b) systematically inspected parameter space such as hypocenter location, depth, and fault dip angle and examined how they affected the ΔCFS assessment result; (c) applied a more reasonable permeability model than most of the other models; (d) pointed out the possibility of indirect triggering due to significant unclamping in the upper part of the fault zone; and (e) demonstrated possible diffusive effect on seismicity by a unique illustration of the relationship of earthquakes versus space and time. We have reached the following conclusions:

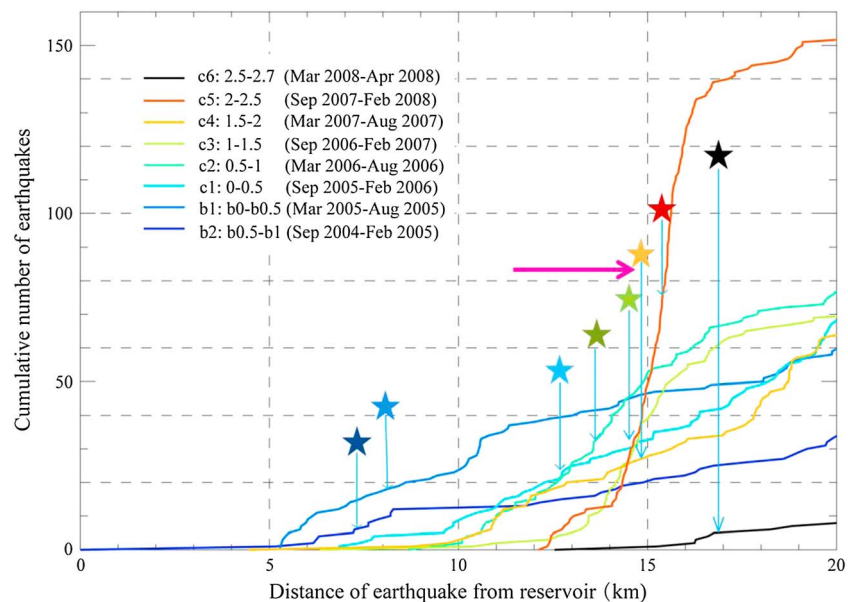


Figure 9. Cumulative histogram of earthquakes versus distance from the ZR. Colors of the curves denote the time ranges at 6 month intervals, except the black curve which represents data of the last 3 months prior to the WE. The stars denote the midpoints of the ranges with steepest slope (i.e., highest seismicity rate) of the curves. The figure shows gradual expansion of a high seismicity rate region from the ZR since its impoundment, a pattern consistent with pore pressure-induced seismicity rate changes.

1. The impoundment of the ZR broke the balance of pore pressure in the region and formed a pore pressure front that slowly propagated through the crust with fluid diffusion, resulting in significant pore pressure increase for the shallow to middle depth (>10 kPa within 10 km of depth) of the LSF underneath the ZR prior to the WE.
2. At initial impoundment, the ΔCFS around the shallow part of the LSF was negative. With the pore pressure growth spreading from the ZR to the surrounding crust, the effective normal stress on nearby LSF reversed from negative to positive and grew outward with time, and the ΔCFS around the LSF region increased progressively. At the time prior to the WE, the ΔCFS increased significantly on a large area of the LSF underneath the ZR from shallow to middle depth (~ 9.3 – 69.1 kPa increase in the depth range of 1–8 km), overlapping with the location of two asperities ruptured during the WE.
3. The impoundment of ZR perhaps did not cause significant increase of the ΔCFS at the hypocenter of the WE, therefore might not have directly triggered the initial rupture of the quake. However, because the reservoir loading significantly increased the ΔCFS on the middle-shallow depth of the LSF and advanced ~ 60 – 450 years of its earthquake recurrence time, a small event in the deeper part of the fault zone could trigger rupture of the asperities above, followed by cascade failure of asperities along the fault zone.
4. The temporal evolution of the microseismicities around the ZR showed an expanding pattern from the ZR since its impoundment, which is consistent with the pattern of pore pressure diffusion due to the ZR, suggesting poroelastic triggering of the microseismic events, and significance of the ZR impoundment on loading the regional tectonic stress field prior to the WE.

Acknowledgments

The authors thank Editor Robert Nowack, the Associate Editor, Christian Klose, and an anonymous review for their thoughtful and constructive comments. The authors were also benefited from discussions with Min Wang, Jianbao Sun, and Xueze Wen. This project was supported in part by grants of NSFC 41090294 and 41374103, CEA LED2008A05, LED2013A04, and LED2009A02, NSF EAR 0911762 and EAR 0911466, and NASA ESI 1468758. Academic licensing for the Abaqus software was provided by Dassault Systemes, Simulia Inc. Chen Jihui of Institute of Geology, CEA provided the aftershock data of the Wenchuan earthquake. Ma Wentao of Institute of Geology, CEA provided the microseismicity data in the vicinity of the Zipingpu reservoir. This work was also partially supported by an NSF I/RD grant (EAR-1323052) for the corresponding author as a rotator program director at NSF. Any opinion, findings, and conclusions or recommendations expressed in this material are those of the author(s) and do not necessarily reflect the views of the National Science Foundation.

References

- Burchfiel, B. C., L. H. Royden, R. D. vander Hilst, B. H. Hager, Z. Chen, R. W. King, C. Li, J. Lü, H. Yao, and E. Kirby (2008), A geological and geophysical context for the Wenchuan earthquake of 12 May 2008, Sichuan People's Republic of China, *Geol. Soc. Am.*, *118*, 7, doi:10.1130/GSATG18A.1.
- Byerlee, J. D. (1978), Friction of rocks, *Pure Appl. Geophys.*, *116*, 615–626.
- Byerlee, J. D. (1992), The change in orientation of subsidiary shears near faults containing pore fluid under high pressure, *Tectonophysics*, *211*, 295–303.
- Cesca, S., B. Dost, and A. Oth (2013), Preface to the special issue “Triggered and induced seismicity: Probabilities and discrimination”, *J. Seismol.*, *17*(1), 1–4.
- Chen, J., Q. Liu, S. Li, B. Guo, Y. Li, J. Wang, and S. Qi (2009), Seismotectonic study by relocation of the Wenchuan M_s 8.0 earthquake sequence [in Chinese with English abstract], *Chin. J. Geophys.*, *52*, 390–397.

- Cocco, M., and J. R. Rice (2002), Pore pressure and poroelasticity effects in Coulomb stress analysis of earthquake interactions, *J. Geophys. Res.*, **107**(B2), 2030, doi:10.1029/2000JB000138.
- Cochran, E. S., J. E. Vidale, and S. Tanaka (2004), Earth tides can trigger shallow thrust fault earthquakes, *Science*, **306**, 1164–1166.
- Cui, X., X. Hu, C. Yu, K. Tao, Y. Wang, and J. Ning (2011), Research on focal mechanism solutions of Wenchuan earthquake sequence, *Acta Sci. Nat. Univ. Pekinensis*, **6**, 1063–1072.
- Dahm, T., et al. (2013), Recommendation for the discrimination of human-related and natural seismicity, *J. Seismol.*, **17**(1), 197–202.
- Deng, K., S. Zhou, R. Wang, R. Robinson, C. Zhao, and W. Cheng (2010), Evidence that the 2008 M_w 7.9 Wenchuan earthquake could not have been induced by the Zipingpu reservoir, *Bull. Seismol. Soc. Am.*, **100**(5B), 2805–2814, doi:10.1785/0120090222.
- Densmore, A. L., M. A. Ellis, Y. Li, R. Zhou, G. S. Hancock, and N. Richardson (2007), Active tectonics of the Beichuan and Pengguan faults at the eastern margin of the Tibetan Plateau, *Tectonics*, **26**, TC4005, doi:10.1029/2006TC001987.
- Durham, W. B. (1997), Laboratory observations of the hydraulic behavior of a permeable fracture from 3800 m depth in the KTB pilot hole, *J. Geophys. Res.*, **102**(B8), 18,405–18,416, doi:10.1029/96JB02813.
- Fielding, E. J., et al. (2013), Kinematic fault slip evolution source models of the 2008 M_w 7.9 Wenchuan earthquake in China from SAR interferometry, GPS and teleseismic analysis and implications for Longmen Shan tectonics, *Geophys. J. Int.*, **194**(2), 1138–1166, doi:10.1093/gji/ggt155.
- Gahalaut, K., and V. K. Gahalaut (2010), Effect of the Zipingpu reservoir impoundment on the occurrence of the 2008 Wenchuan earthquake and local seismicity, *Geophys. J. Int.*, **183**, 277–285.
- Ge, S. (2011), Comment on “Evidence that the 2008 M_w 7.9 Wenchuan earthquake could not have been induced by the Zipingpu reservoir” by Kai Deng, Shiyong Zhou, Rui Wang, Russell Robinson, Cuiping Zhao, and Wanzheng Cheng, *Bull. Seismol. Soc. Am.*, **101**(6), 3117–3118, doi:10.1785/0120110066.
- Ge, S., M. Liu, N. Lu, J. W. Godt, and G. Luo (2009), Did the Zipingpu reservoir trigger the 2008 Wenchuan earthquake?, *Geophys. Res. Lett.*, **36**, L20315, doi:10.1029/2009GL040349.
- Guha, S. K. (2000), *Induced Earthquakes*, Kluwer Acad., Dordrecht, Netherlands.
- Guo, X., X. Chen, and Y. Li (2010), Focal mechanism solutions for the 2008 M_s 8.0 Wenchuan earthquake and part of its aftershocks [in Chinese], *Earthquake*, **30**(1), 50–60.
- Gupta, H., and R. Chadha (1995), *Induced Seismicity*, Pure Appl. Geophys., vol. 145, Birkhäuser, Boston, Mass.
- Hagiwara, T., and M. Ohtake (1972), Seismic activity associated with the filling of the reservoirs behind the Kurobe dam, Japan 1963–70, *Tectonophysics*, **15**, 241–254.
- Hainzl S., S. Steacy, and D. Marsan (2010), Seismicity models based on Coulomb stress calculations, Community online resource for statistical seismicity analysis (CORSSA), doi:10.5078/corssa-32035809. [Available at <http://www.corssa.org>.]
- Harris, R. A. (1998), Introduction to special section: Stress triggers, stress shadows, and implications for seismic hazard, *J. Geophys. Res.*, **103**, 24,347–24,358, doi:10.1029/98JB01576.
- Hu X. P., Yu C. Q., Tao K., X. F. Cui, J. Ning, and Y. H. Wang (2008), Focal mechanism solutions of Wenchuan earthquake and its strong aftershocks obtained from initial P wave polarity analysis [in Chinese], *Chin. J. Geophys.*, **51**(6), 1711–1718.
- Ingebritsen, S. E., and C. E. Manning (1999), Geological implications of a permeability-depth curve for the continental crust, *Geology*, **27**, 1107–10.
- Ingebritsen, S. E., and C. E. Manning (2010), Permeability of the continental crust: Dynamic variations inferred from seismicity and metamorphism, *Geofluids*, **10**, 193–205, doi:10.1111/j.1468-8123.2010.00278.x.
- Jia, D., Y. Q. Li, A. M. Lin, M. M. Wang, W. Chen, X. J. Wu, Z. K. Ren, Y. Zhao, and L. Luo (2010), Structural model of 2008 M_w 7.9 Wenchuan earthquake in the rejuvenated Longmen Shan thrust belt, China, *Tectonophysics*, **491**, 174–184, doi:10.1016/j.tecto.2009.08.040.
- Kalpna, and R. Chander (2000), Green’s function based stress diffusion solution in the porous elastic half space for time varying finite reservoir loads, *Phys. Earth Planet. Inter.*, **120**, 93–101.
- Kerr, R., and R. Stone (2009), A human trigger for the great quake of Sichuan?, *Science*, **323**, 322, doi:10.1126/science.323.5912.322.
- King, G. C. P., R. S. Stein, and J. Lin (1994), Static stress changes and the triggering of earthquakes, *Bull. Seismol. Soc. Am.*, **84**, 935–953.
- Klose, C. D. (2008), The 2008 M_w 7.9 Wenchuan earthquake—Result of local and abnormal mass imbalances? *Eos Trans. AGU*, **89**(53), Fall Meet. Suppl., Abstract U21C-08.
- Klose, C. D. (2012), Evidence for anthropogenic surface loading as trigger mechanism of the 2008 Wenchuan earthquake, *Environ. Earth Sci.*, **66**, 1439–1447, doi:10.1007/s12665-011-1355-7.
- Kusalaria, J., and P. Talwani (1992), The role of elastic, undrained, and drained responses in triggering earthquakes at Monticello Reservoir, South Carolina, *Bull. Seismol. Soc. Am.*, **82**, 1867–1888.
- Lei, X. (2010), Possible roles of the Zipingpu reservoir in triggering the 2008 Wenchuan earthquake, *J. Asian Earth Sci.*, **40**(4), 844–854, doi:10.1016/j.jseae.2010.05.004.
- Lei, X., S. Ma, X. Wen, J. Su, and F. Du (2008), Integrated analysis of stress and regional seismicity by surface loading—A case study of Zipingpu reservoir [in Chinese with English abstract], *Seismol. Geol.*, **30**(4), 1046–1064.
- Li, H., et al. (2013), Characteristics of the fault-related rocks, fault zones and the principal slip zone in the Wenchuan Earthquake Fault Scientific Drilling Project Hole-1 (WFSD-1), *Tectonophysics*, **584**, 23–42.
- Ma, W., C. Xu, X. Zhang, X. Xu, H. Li, and J. Yuan (2011), Study on the relationship between the reservoir induced seismicity at Zipingpu reservoir and the M 8.0 Wenchuan earthquake [in Chinese with English abstract], *Seismol. Geol.*, **33**(1), 175–190, doi:10.3969/j.issn.0253-4967.2011.01.017.
- Miller, S. A. (2013), The role of fluids in tectonic and earthquake processes, *Adv. Geophys.*, **54**, 1–46.
- Roeloffs, E. A. (1988), Fault stability changes induced beneath a reservoir with cyclic variations in water level, *J. Geophys. Res.*, **93**, 2107–2124, doi:10.1029/JB093iB03p02107.
- Shen, Z.-K., J. Lu, M. Wang, and R. Burgmann (2005), Contemporary crustal deformation around southeast borderland of Tibetan plateau, *J. Geophys. Res.*, **110** B11409, doi:10.1029/2004JB003421.
- Shen, Z.-K., J. Sun, P. Zhang, Y. Wan, M. Wang, R. Burgmann, Y. Zeng, W. Gan, H. Liao, and Q. Wang (2009), Slip maxima at fault junctions and rupturing of barriers during the 2008 Wenchuan earthquake, *Nat. Geosci.*, **2**, 718–724.
- Shmonov, V. M., V. M. Vitvotova, A. V. Zharikov, and A. A. Grafchikov (2003), Permeability of the continental crust: Implications of experimental data, *J. Geochem. Explor.*, **78–79**, 697–699.
- Stein, R. S. (1999), The role of stress transfer in earthquake occurrence, *Nature*, **402**, 605–609.
- Talwani, P. (1997), The nature of reservoir-induced seismicity, *Pure Appl. Geophys.*, **150**, 473–492, doi:10.1007/s000240050089.
- Talwani, P., and S. Acree (1984), Pore press diffusion and the mechanism of reservoir-induced seismicity, *Pure Appl. Geophys.*, **122**, 947–965.
- Turcotte, D. L., and G. Schubert (2002), *Geodynamics: Applications of Continuum Physics to Geological Problems*, 2nd ed., 528 pp., Cambridge Univ. Press, Cambridge.

- Wang, H. F. (2000), *Theory of Linear Poroelasticity: With Applications to Geomechanics and Hydrogeology*, Princeton Univ. Press, Princeton and Oxford.
- Wang, Q., X. Qiao, Q. Lan, J. Freymueller, S. Yang, C. Xu, Y. Yang, X. You, K. Tan, and G. Chen (2011), Rupture of deep faults in the 2008 Wenchuan earthquake and uplift of the Longmen Shan, *Nat. Geosci.*, *31*, doi:10.1038/NCEO1210.
- Wang, Y., F. Wang, M. Wang, Z. Shen, and Y. Wan (2014), Coulomb stress change and evolution induced by the 2008 Wenchuan earthquake and its delayed triggering of the 2013 M_w 6.6 Lushan earthquake, *Seismol. Res. Lett.*, *85*(1), 52–59, doi:10.1785/0220130111.
- Xu, X., X. Wen, G. Yu, G. Chen, Y. Klinger, J. Hubbard, and J. Shaw (2009), Coseismic reverse- and oblique-slip surface faulting generated by the 2008 M_w 7.9 Wenchuan earthquake, China, *Geology*, *37*(6), 515–518, doi:10.1130/G25462A.1.
- Yang, Z., Y. Chen, J. Su, T. Chen, and P. Wu (2012), The hypocenter and origin time of the M_w 7.9 Wenchuan earthquake of May 12, 2008 [in Chinese], *Acta Seismol. Sin.*, *34*(2), 127–136.
- Zhang, P.-Z., et al. (2004), Continuous deformation of the Tibetan plateau from global positioning system data, *Geology*, *32*, 809–812.
- Zhang, P. Z., X. Z. Wen, Z.-K. Shen, and J. H. Chen (2010), Oblique, high-Angle, listric-reverse faulting and associated development of strain: The Wenchuan earthquake of May 12, 2008, Sichuan, China, *Annu. Rev. Earth Planet. Sci.*, *38*, 351–80.
- Zhou, S., and K. Deng (2011), Reply to "Comment on 'Evidence that the 2008 M_w 7.9 Wenchuan earthquake could not have been induced by the Zipingpu reservoir' by Kai Deng, Shiyong Zhou, Rui Wang, Russell Robinson, Cuiping Zhao, and Wanzheng Cheng" by Shemin Ge, *Bull. Seismol. Soc. Am.*, *101*(6), 3119–3120, doi:10.1785/0120110099.